



A Low-Cost Lightweight Entropic Alloy with High Strength

Lei Shao, Tao Zhang, Lugee Li, Yuhong Zhao, Jinfeng Huang, Peter K. Liaw, and Yong Zhang

(Submitted April 11, 2018; in revised form August 23, 2018; published online October 31, 2018)

In this study, a series of lightweight Al–Mg system entropic alloys containing Zn, Cu, and Si were designed based on the order/disorder or entropy, and eutectic concepts. The alloys of $\text{Al}_{58.5}\text{Mg}_{31.5}\text{Zn}_{4.5}\text{Cu}_{4.5}\text{Si}_1$; $\text{Al}_{63}\text{Mg}_{27}\text{Zn}_{4.5}\text{Cu}_{4.5}\text{Si}_1$; $\text{Al}_{66.7}\text{Mg}_{23.3}\text{Zn}_{4.5}\text{Cu}_{4.5}\text{Si}_1$; $\text{Al}_{80}\text{Mg}_{14}\text{Zn}_{2.7}\text{Cu}_{2.7}\text{Si}_{0.6}$; $\text{Al}_{85}\text{Mg}_{10.5}\text{Zn}_{2.025}\text{Cu}_{2.025}\text{Si}_{0.45}$; and $\text{Al}_{90}\text{Mg}_7\text{Zn}_{1.35}\text{Cu}_{1.35}\text{Si}_{0.3}$ were prepared by induction melting under a high-purity argon atmosphere and then casted into stainless steel molds. The microstructures which were tested in the as-cast state exhibited multiphases and contained apparent volume fractions of intermetallic compounds and solid solutions. Then, the compressive mechanical properties of the alloys were measured, and high fracture strengths of 577, 677, 590, 498, 814, and 794 MPa, respectively, were determined. Strong hardening phenomena were observed in the $\text{Al}_{80}\text{Mg}_{14}\text{Zn}_{2.7}\text{Cu}_{2.7}\text{Si}_{0.6}$, $\text{Al}_{85}\text{Mg}_{10.5}\text{Zn}_{2.025}\text{Cu}_{2.025}\text{Si}_{0.45}$, and $\text{Al}_{90}\text{Mg}_7\text{Zn}_{1.35}\text{Cu}_{1.35}\text{Si}_{0.3}$ alloys at room temperature, with amazing plasticity percentages of 13.8, 24.8, and 32.7%, respectively. The property differences in the lightweight alloys were analyzed using the following parameters: the critical values of the enthalpy of mixing; atomic size differences; ratio of entropy to enthalpy; valence electron concentration (VEC); and Pauling electronegativity difference. Finally, three of the aforementioned parameters (atomic size difference, enthalpy of mixing, and Pauling electronegativity difference) were regarded in this study as the crucial rules for the lightweight multicomponent alloys.

Keywords Al–Mg medium entropic alloy, critical values, lightweight, mechanical properties

1. Introduction

A new class of entropic alloys (also referred to as nonlinear alloys) was first proposed by Yeh et al. in 1995, and alloys with outstanding properties were prepared in 2004 (Ref 1). HEAs may be defined as containing multiple principle elements, and the atomic percentages of each element range between 5 and 35% (Ref 2). Due to the benefits of the high entropy of mixing, HEAs have the ability to resist the effects of mixing enthalpy and restrain the precipitation of ordered intermetallic compounds. Therefore, when cooling from the molten state, HEAs are intended to form simple, disordered, face-centered cubic

(FCC), body-centered cubic (BCC), or hexagonal close-packed (HCP) solid solutions rather than ordered phases (Ref 3–8). And, according to the previous study results, the HEAs can possess comprehensive properties which may not be available in other traditional alloys (Ref 9–26). Therefore, since they provide a new alloy designing concept, the HEAs may be marked as a milestone in the development of structural and functional metallic materials. In particular, due the aforementioned positive properties, the HEAs have greatly expanded the current vast applicable alloy systems.

The low-density HEAs which have been investigated in recent years are considered to be important lightweight materials with high strength (Ref 27, 28). Youssef et al. studied low-density nanostructured HEAs (grain size: approximately 12 nm) $\text{Li}_{20}\text{Al}_{20}\text{Mg}_{10}\text{Sc}_{20}\text{Ti}_{30}$ using a mechanical alloying technique (Ref 29). The alloys exhibited a single FCC phase structure, with a high hardness (5.9 GPa). It was observed that after annealing at 500 °C, the crystal structures transformed to a HCP phase structures, and the hardness decreased to 4.9 GPa. In order to meet the demands of the aerospace industry, Senkov et al. (Ref 30, 31) designed low-density refractory Cr–Nb–Ti–V–Zr alloy systems using vacuum arc melting, followed by hot isostatic pressing (HIP) and homogenization annealing, which exhibited densities in the range of 6.34 g/cm^{-3} (NbTiV₂Zr) to 6.67 g/cm^{-3} (CrNbTiZr). They found that the CrNiTiVZr alloy had more attractive properties than that the In718 and Haynes 230 alloys. However, the density was found to be significantly high, and further weight reduction was required for lightweight applications. An AlTiVCr equiatomic alloy with a single-phase structure was prepared by Qiu et al. (Ref 32). The density of the alloy was 5.06 g/cm^3 . In another related study, Li et al. examined $\text{Mg}_x(\text{AlCuMnZn})_{100-x}$ HEAs using induction melting and casting in copper molds (Ref 33, 34). The alloys exhibited mainly HCP phases and Al–Mn icosahedral quasicrystalline phases, with densities ranging from 2.20 to 4.29 g/cm^{-3} depending on the percentage of Mg in the composition. Those alloys showed the compression strengths of 400 to 500 MPa

This article is an invited paper selected from presentations at “AeroMat 2017,” held April 10–12, 2017, in Charleston, South Carolina, and has been expanded from the original presentation.

Lei Shao and **Jinfeng Huang**, State Key Laboratory for Advanced Metals and Materials, University of Science and Technology Beijing, No. 30, Xueyuan Road, Beijing 100083, People’s Republic of China; **Tao Zhang** and **Lugee Li**, Dongguan Eontech Co Ltd, Dongguan 523662, Guangdong, People’s Republic of China; **Yuhong Zhao**, College of Materials Science and Engineering, North University of China, No. 3, Xueyuan Road, Taiyuan 030051, People’s Republic of China; **Peter K. Liaw**, Department of Materials Science and Engineering, The University of Tennessee, Knoxville, TN 37996; and **Yong Zhang**, State Key Laboratory for Advanced Metals and Materials, University of Science and Technology Beijing, No. 30, Xueyuan Road, Beijing 100083, People’s Republic of China; and Beijing Key Laboratory for Magneto-Photoelectrical Composite and Interface Science, University of Science and Technology Beijing, No. 30, Xueyuan Road, Beijing 100083, People’s Republic of China. Contact e-mail: drzhangy@ustb.edu.cn.

and the ductilities of 3-5% at room temperature. Beak et al. reported the microstructures and compressive properties of Al₇₀Mg₁₀Si₁₀Cu₅Zn₅ alloys at room and elevated temperatures (Ref 35-37). An ultrasonic melt treatment (UST) was used to improve the ultimate compressive strength of as-cast alloys from 573 to 681 MPa, since the USTs could effectively decrease both the grain sizes and precipitated phase sizes. Then, the precipitation behaviors of the Al-6Mg-9Si-10Cu-10Zn-3Ni alloys were investigated, along with their impacts on the compressive strength. The mechanical properties were found to be greatly improved, causing fine clusters and precipitates to be formed at below 70 °C. The Al-6Mg-9Si-10Cu-10Zn-3Ni alloys showed excellent mechanical properties (> 700 MPa) when compared to some of the Al alloys (A356 and A390). In another related study conducted by Yang et al. (Ref 38), heavy elements were substituted for the Al, Li, and Mg light elements in Al-Li-Mg systems. It was found that the densities varied from 2.84 g/cm³ (Al₈₀Li₅Mg₅Zn₅Sn₅) to 3.88 g/cm³ (Al-LiMgZnSn). However, the resulting microstructures were multi-phased, with numerous intermetallic phases observed.

In order to develop advanced lightweight alloys, a series of low-density multicomponent alloys based on the Al-Mg system were investigated according to a high-entropy strategy (Ref 2, 39-44). In accordance with the results of the previous studies (Ref 38), the content levels of zinc, copper, and silicon were designed to a 10% mole fraction. In this study, from the perspective of a ternary phase diagram, a straight line could be drawn which joined two points, Al₆₂Mg₃₈ and ZnCuSi. The schematic is shown in Fig. 1. The point of the Al₆₂Mg₃₈ was decided due to its eutectic point of Al-Mg system alloys. The eutectic point displayed the best fluidity and casting properties. The aforementioned line intersected the line of 10 atomic percent (at.%) content of zinc, copper, and silicon at the A₁ (Al_{58.5}Mg_{31.5}Zn_{4.5}Cu_{4.5}Si₁) point. Next, the other two points, A₂ (Al₆₃Mg₂₇Zn_{4.5}Cu_{4.5}Si₁) and A₃ (Al_{66.7}Mg_{23.3}Zn_{4.5}Cu_{4.5}Si₁), were chosen in the line of 10 at.% content of zinc, copper, and silicon. After examining the comprehensive mechanical properties of the three points, it was found that the A₃ point displayed better properties than the other two points. Therefore, points A₁ and A₃ were connected, and the content of B₁

(Al₈₀Mg₁₄Zn_{2.7}Cu_{2.7}Si_{0.6}), B₂ (Al₈₅Mg_{10.5}Zn_{2.025}Cu_{2.025}Si_{0.45}), and B₃ (Al₉₀Mg₇Zn_{1.35}Cu_{1.35}Si_{0.3}) was selected. The microstructure, phase composition, and mechanical behaviors were described herein.

2. Experimental Procedures

In this study, the Al-Mg-based medium entropic alloys were produced by the vacuum induction melting of the simple mixtures of the corresponding elements under a high-purity argon atmosphere in a graphite crucible. All of the raw materials were in bulk form, with a purity of 99.9 weight percent (wt.%). Prior to placing in the crucible, all of the elements were polished using a grinding machine in order to remove the oxide film. Then, to achieve a homogeneous distribution of the elements in the alloys, each alloy was remelted several times in order to guarantee a total of 30 min in a liquid state. The molten alloys were then cast into a Φ75 mm × 10 mm steel mold.

All of this study's tests were carried out in the as-cast condition. The phase formation was determined by x-ray diffraction (XRD) using a SmartLab diffractometer with Cu-α radiation. Then, specimens with dimensions of 8 × 8 × 10 mm³ were ground, polished, and etched by a Keller reagent for subsequent microstructure observations. The microstructures were characterized by a ZEISS SUPRA 55 scanning electron microscope (SEM) which was installed with an energy-dispersive spectrometer (EDS). Compression tests with a strain rate of 1 × 10⁻³ s⁻¹ at room temperature were carried out on cylindrical samples (3 mm in diameter and 6 mm in length), which had been cut from the casted alloys using an electric discharged machine. For the compression tests, the cylindrical samples were carefully polished, and at least three specimens were tested for each alloy in order to obtain the statistical distributions of the tensile properties. The densities of the alloys were measured using an Archimedes method.

3. Results

3.1 Densities of the Alloys

The densities (ρ) of the targeted alloys were measured using an Archimedes method, as detailed in Table 1.

A rule of mixture assumption of a solid solution was used for examining the targeted alloys, and the estimated theoretical densities (ρ_{mix}) are listed in Table 1 (Ref 45-47):

$$\rho_{\text{mix}} = \frac{\sum_{i=1}^n c_i A_i}{\sum_{i=1}^n c_i A_i / \rho_i} \quad (\text{Eq 1})$$

where c_i , A_i , and ρ_i are the weight fraction, atomic weight, and density of the i th corresponding element, respectively, and n denotes the total number of elements. It was found that when comparing the measured density and corresponding theoretical mixed densities, significant deviations were observed, which suggested that ordered intermetallic compounds were present.

3.2 Phase Formations and Microstructures

The results of this study's x-ray diffraction and corresponding backscattered electron images are shown in Fig. 2 and 3,

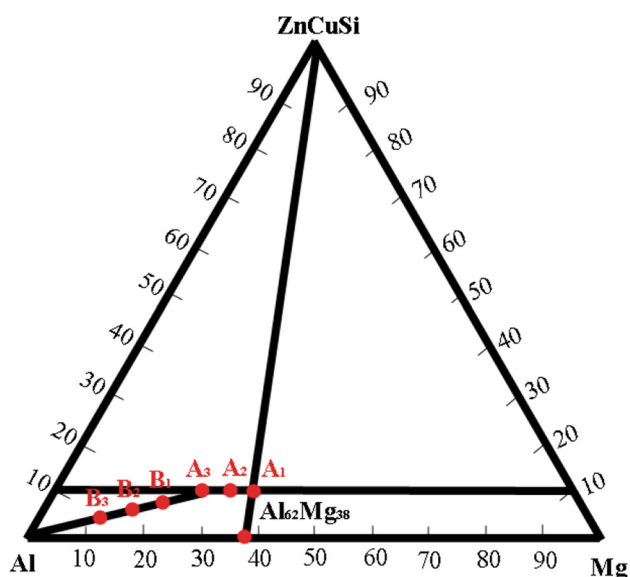
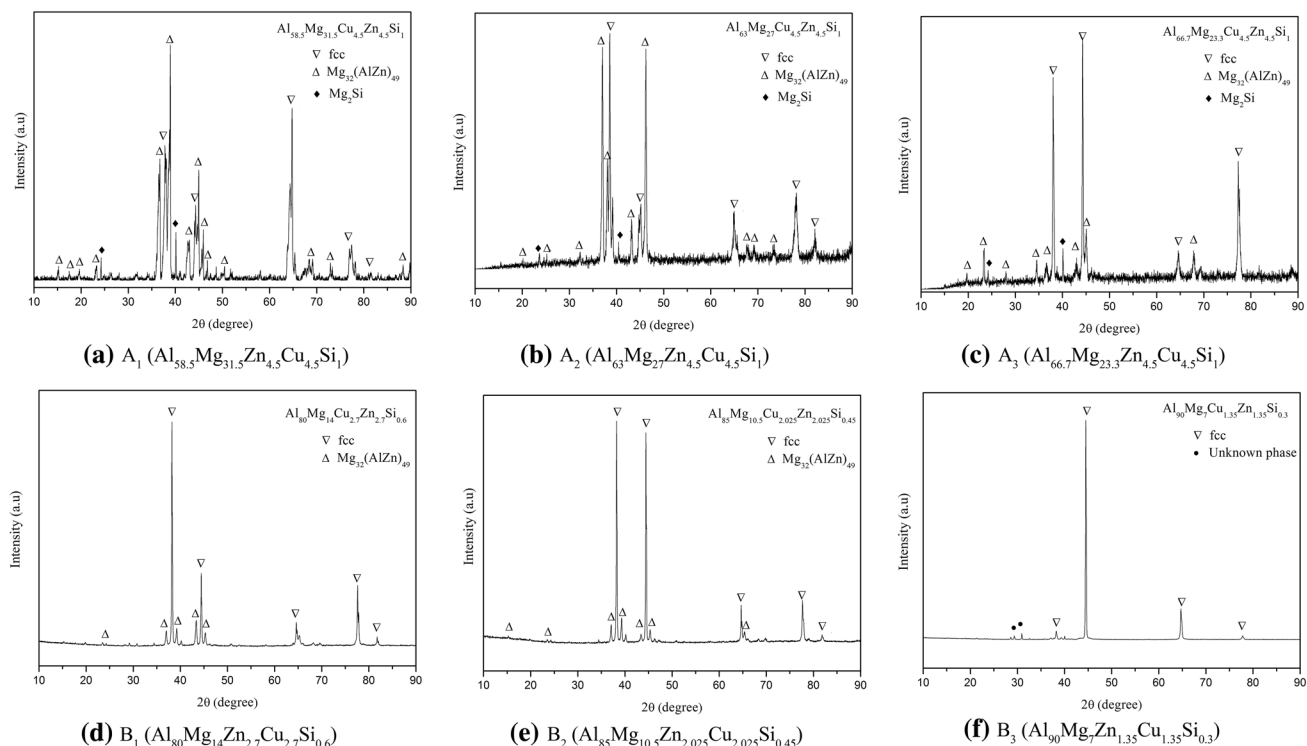


Fig. 1 Design schematic of Al-Mg-based multicomponent alloy

Table 1 Chemical compositions (at.%) and densities (ρ) of alloys in this work

Alloy	Al	Mg	Cu	Zn	Si	ρ , g/cm ⁻³	ρ_{mix} , g/cm ⁻³
A ₁ (Al _{58.5} Mg _{31.5} Zn _{4.5} Cu _{4.5} Si ₁)	59.94	28.31	5.71	4.03	2.01	2.64	2.66
A ₂ (Al ₆₃ Mg ₂₇ Zn _{4.5} Cu _{4.5} Si ₁)	65.26	23.94	5.66	3.92	1.22	2.69	2.74
A ₃ (Al _{66.7} Mg _{23.3} Zn _{4.5} Cu _{4.5} Si ₁)	71.11	17.74	6.07	3.75	1.33	2.75	2.77
B ₁ (Al ₈₀ Mg ₁₄ Zn _{2.7} Cu _{2.7} Si _{0.60})	83.05	9.85	3.04	2.29	1.77	2.73	2.58
B ₂ (Al ₈₅ Mg _{10.5} Zn _{2.025} Cu _{2.025} Si _{0.45})	87.77	7.72	2.63	1.64	0.23	2.72	2.66
B ₃ (Al ₉₀ Mg _{7.1} Zn _{1.35} Cu _{1.35} Si _{0.3})	91.47	5.35	2.02	0.96	0.20	2.71	2.72

**Fig. 2** XRD patterns of as-cast lightweight Al-Mg-based multicomponent alloys

respectively. All of the major phases are identified in Fig. 2. Meanwhile, the phase compositions of the alloys were found to be complex, not only in regard to the solid solution phases, but also the intermetallic phases. Furthermore, the scanning electron micrographs were also complex, with at least two constituents observed in each alloy. Moreover, remarkable differences were observed between the fabricated alloys. The compositions of the phases measured by the EDS analysis are listed in Table 2.

Figure 2(a) details the XRD pattern of the A₁ alloy. When comparing the alloy with traditional HEAs with BCC and/or FCC phases, it was not surprising to find them to be more complex (Ref 48-51). The ordered Mg₃₂(AlZn)₄₉ and Mg₂Si phases, along with a solid solution phase, were observed in the diffraction graph of the alloy. In this study, the intensity of the diffraction peak of the ordered intermetallic phase was considered as the strongest and was obviously higher than the second and the third peaks of the FCC solid solution phases, which indicated that the intermetallic phase was the dominant phase. The SEM images of the A₁ alloy are shown in Fig. 3(a), in which five constituents (marked as A, B, C, D, and E, respectively) with different contrasts are evident. The phase

constituents of the various regions were identified by EDS analysis, and the results are listed in Table 2. Then, combined with the EDS analysis results, the phase constituents of each region in the A₁ alloy were successfully identified. It was believed that Region A was most probably the Mg₃₂(AlZn)₄₉ phase, and Region B was a matrix of the α -Al based solid solution. The black rhombic (marked as C in the figure) denoted the Mg₂Si phase. Region D was the eutectic phase, and Region E contained the segregation elements of Cu and Zn.

The XRD pattern of the A₂ alloy is shown in Fig. 2(b). The A₂ alloy was similar to the A₁ alloy and composed of the FCC phase, Mg₃₂(AlZn)₄₉ and Mg₂Si. However, the intensities of ordered phases were weaker than those detailed in Fig. 2(a), which suggested that the volume fraction of the ordered phases had been decreased. The microstructure of the A₂ alloy is presented in Fig. 3(b), in which four different constituents are evident and marked as A, B, C, and D. In this study, in accordance with the microstructure and EDS results listed in Table 2, it was indicated that Region A was probably the Mg₂Si; Region B was a α -Al based solid solution; and Region D was a typical eutectic structure. When compared with the A₁ alloy, the eutectic phase in the A₂ alloy displayed a higher

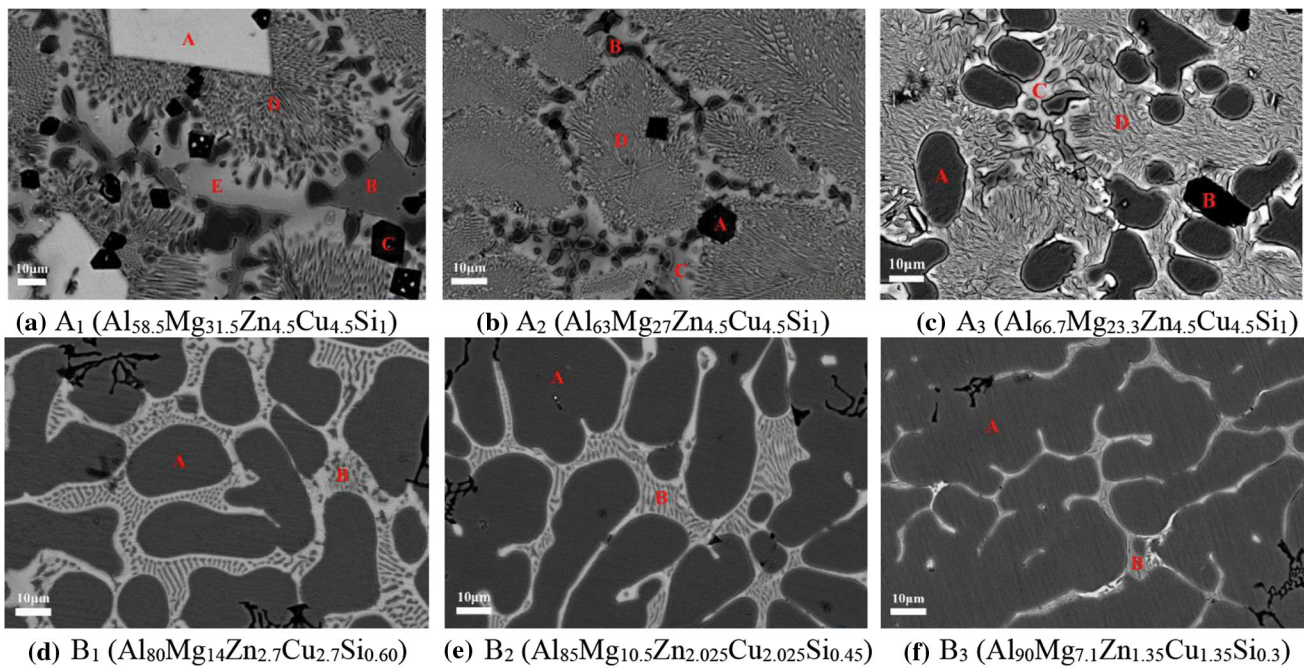


Fig. 3 SEM backscattered electron images of as-cast lightweight Al-Mg-based multicomponent alloy

Table 2 Chemical compositions (at.%) of phases identified in the microstructures of $\text{Al}_{55.8}\text{Mg}_{34.2}\text{Zn}_{4.5}\text{Cu}_{4.5}\text{Si}_1$, $\text{Al}_{63}\text{Mg}_{27}\text{Zn}_{4.5}\text{Cu}_{4.5}\text{Si}_1$, $\text{Al}_{66.7}\text{Mg}_{23.3}\text{Zn}_{4.5}\text{Cu}_{4.5}\text{Si}_1$, $\text{Al}_{80}\text{Mg}_{14}\text{Zn}_{2.7}\text{Cu}_{2.7}\text{Si}_{0.6}$, $\text{Al}_{85}\text{Mg}_{10.5}\text{Zn}_{2.025}\text{Cu}_{2.025}\text{Si}_{0.45}$, and $\text{Al}_{90}\text{Mg}_{7.1}\text{Zn}_{1.35}\text{Cu}_{1.35}\text{Si}_{0.3}$

Alloy	Region	Composition, at.%				
		Al	Mg	Cu	Zn	Si
A_1 ($\text{Al}_{58.5}\text{Mg}_{31.5}\text{Zn}_{4.5}\text{Cu}_{4.5}\text{Si}_1$)	A	46.31	35.57	11.50	6.62	...
	B	85.69	12.78	0.50	1.03	...
	C	4.06	23.93	0.44	0.91	70.66
	D	75.30	19.33	3.15	2.22	...
	E	58.43	31.12	5.29	5.16	...
A_2 ($\text{Al}_{63}\text{Mg}_{27}\text{Zn}_{4.5}\text{Cu}_{4.5}\text{Si}_1$)	A	1.63	58.27	40.11
	B	85.11	13.65	0.34	0.9	...
	C	60.39	28.27	6.72	4.62	...
	D	64.13	24.46	7.34	4.06	...
A_3 ($\text{Al}_{66.7}\text{Mg}_{23.3}\text{Zn}_{4.5}\text{Cu}_{4.5}\text{Si}_1$)	A	88.65	9.28	0.72	1.35	...
	B	2.92	52.37	0.65	0.51	43.55
	C	65.32	20.34	8.77	5.23	0.33
	D	62.48	22.41	9.63	5.22	0.27
B_1 ($\text{Al}_{80}\text{Mg}_{14}\text{Zn}_{2.7}\text{Cu}_{2.7}\text{Si}_{0.6}$)	A	90.98	6.93	0.58	1.50	0.00
	B	58.94	21.14	13.49	6.29	0.14
B_2 ($\text{Al}_{85}\text{Mg}_{10.5}\text{Zn}_{2.025}\text{Cu}_{2.025}\text{Si}_{0.45}$)	A	92.54	5.82	0.59	1.05	...
	B	47.78	25.67	19.70	6.05	0.8
B_3 ($\text{Al}_{90}\text{Mg}_{7.1}\text{Zn}_{1.35}\text{Cu}_{1.35}\text{Si}_{0.3}$)	A	93.80	4.82	0.47	0.91	0.00
	B	63.36	14.19	18.96	2.96	0.53

volume, which may have been the result of the constituent of the A_2 alloy having a close proximity to the eutectic point.

When the content of the aluminum reached 66.7 at.%, there are no changes observed in the types of phases in the A_3 alloy. However, there were decreases observed in the peaks intensities of the ordered intermetallic phases, while the FCC phase became notable (Fig. 2c). There were four distinct alloy constituents found, marked as A, B, C, and D in Fig. 3(c). In accordance with the EDS results shown in Table 2, it was

concluded that Region A corresponded to a α -Al solid solution phase; Region B was Mg_2Si ; and Regions C and D were similar to Regions C and D in the A_2 alloy, respectively.

The XRD patterns of the Al-Mg-rich alloys, B_1 , B_2 , and B_3 are shown in Fig. 2(d) to (f), respectively. There were two phases [α -Al and $\text{Mg}_{32}(\text{AlZn})_{49}$] recognized in the XRD patterns of the Al-Mg-rich alloys. It was found that with the increases in aluminum content, the intensities of the peaks of the α -Al became stronger, while those of the $\text{Mg}_{32}(\text{AlZn})_{49}$

became weaker. Eventually, only the α -Al phase could be identified in the B₃ alloys containing 90 at.% aluminum. Those alloys were determined to be composed of the FCC phase as the major phase, and the ordered phase of the Mg₃₂(AlZn)₄₉ or unknown phases were considered to be minor phases. The SEM images of the aforementioned alloys are presented in Fig. 3(d) to (f), respectively. The Al-Mg-rich alloys displayed thick dendritic structures. It was observed that the higher the aluminum content was, the thicker the dendrite would be, and the matrix was divided by the eutectic structure. When combined with the EDS analysis results listed in Table 2, the eutectic regions were determined to be rich in Mg, Cu, and Zn, which may have been Mg₃₂(AlZn)₄₉ or other unknown phases. However, the B regions in Fig. 3(d) to (f) were found to be Cu enriched. This trend suggested that, due to a higher melting temperature, the element Cu had segregated during the solidification process.

3.3 Mechanical Behavior

Figure 4 details the compressive stress–strain curves for the as-cast alloys at room temperature. The engineering properties of these alloys are listed in Table 3. During this study’s compression testing at room temperature, the A₁, A₂, and A₃ alloys failed without obvious yielding. It was found that they had fractured by shattering into many pieces after approaching the maximum strengths of 577 MPa, 676 MPa, and 660 MPa at the engineering strains of 3.2, 1.9, and 4.2%, respectively. The test results revealed that these alloys exhibited high compressive strength (exceeding 550 MPa), but very low plasticity. The room temperature compression behaviors of the B₁, B₂, and B₃ alloys were found to be different from those described above. These alloys displayed plastic yielding at $\sigma_{0.2} = 203, 255,$ and 198 MPa, respectively. After that, a continuous increase in their strengths occurred with increases in the compression strain. For example, the strengths of the B₂ and B₃ alloys had increased to $\sigma_{20} = 721$ MPa and 669 MPa, respectively, after compression by 20% at room temperature. It was observed that with the increases in the aluminum content, the engineering strain had greatly improved from 1.9 to 32.7%. The B₁ alloy fracture strength (σ_f) had decreased to 498 MPa. However, that of the B₂ and B₃ alloys had approached or exceeded 800 MPa and

displayed excellent room temperature compressive strengths. In other words, the plasticity of these alloys had been improved by increasing the aluminum content and the volume fraction of the more ductile α -Al phase.

4. Discussion

From the viewpoint of the thermodynamic concept, a system will attempt to minimize its Gibbs free energy (ΔG_{mix}) in order to achieve a metastable or stable equilibrium state, which is known to be related to the enthalpy (ΔH_{mix}) and entropy (ΔS_{mix}). The Gibbs free energy formula is shown in Eq 2:

$$\Delta G_{\text{mix}} = \Delta H_{\text{mix}} - T\Delta S_{\text{mix}} \quad (\text{Eq 2})$$

It can be seen that the Gibbs free energy (ΔG_{mix}) is determined by the enthalpy of the mixing (ΔH_{mix}) and the entropy of the mixing (ΔS_{mix}) at a given temperature (T) for an equilibrium state. It is the competition result between the ΔH_{mix} and $T\Delta S_{\text{mix}}$, which affects the phase selection in the HEAs.

Furthermore, the mixing enthalpy and entropy are two important parameters in the study of HEAs and multicomponent alloys. Therefore, based on the thermodynamic and Hume–Rothery rules for solid solution formations, the phase formations in HEAs can be characterized by some specifically derived parameters, such as the ΔH_{mix} (enthalpy of mixing); δ (atomic size difference); Ω (ratio of entropy to enthalpy); VEC (valance electron concentration); and $\Delta\chi$ (Pauling electronegativity difference). These criteria and related parameters are defined as follows:

$$\Delta S_{\text{mix}} = -R \sum_{i=1}^n c_i \ln c_i \quad (\text{Eq 3})$$

where ΔS_{mix} is the mixing entropy; R is the gas constant; and c_i denotes the atomic percentages of the i th element. The enthalpy of the mixing ΔH_{mix} can be determined as follows:

$$\Delta H_{\text{mix}} = \sum_{i=1}^n \sum_{j=1, i \neq j}^n \Omega_{ij} c_i c_j \quad (\text{Eq 4})$$

where $\Omega_{ij} = 4\Delta H_{\text{mix}} AB$; $\Delta H_{\text{mix}} AB$ is the mixing of the enthalpy of binary equiatomic AB alloys; and Ω_{ij} is the regular melt interaction parameter between the i th and j th elements. Then, the atomic size difference (δ) can be obtained by the following:

$$\delta = \sqrt{\sum_{i=1}^n c_i \left(1 - \frac{r_i}{\bar{r}}\right)^2} \quad (\text{Eq 5})$$

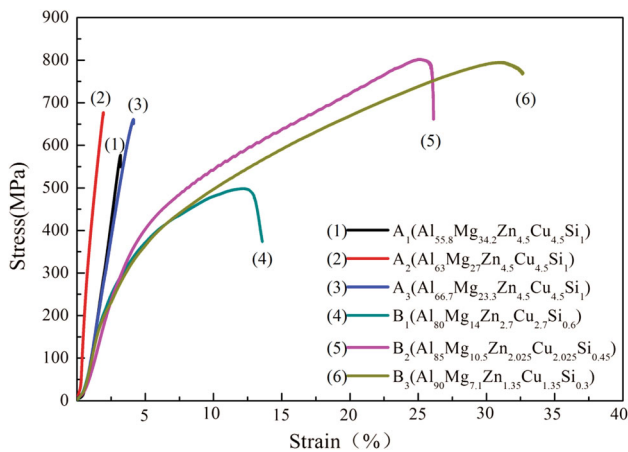


Fig. 4 Compressive stress–strain curves at room temperature. The strain rate is 10^{-3} s^{-1}

Table 3 Compressive mechanical properties of Al–Mg–Zn–Cu–Si alloys

Alloy	$\sigma_{0.2}$, MPa	σ_f , MPa	ϵ_p , %
A ₁ (Al _{58.5} Mg _{31.5} Zn _{4.5} Cu _{4.5} Si ₁)	...	577	3.2
A ₂ (Al ₆₃ Mg ₂₇ Zn _{4.5} Cu _{4.5} Si ₁)	...	676	1.9
A ₃ (Al _{66.7} Mg _{23.3} Zn _{4.5} Cu _{4.5} Si ₁)	...	660	4.2
B ₁ (Al ₈₀ Mg ₁₄ Zn _{2.7} Cu _{2.7} Si _{0.60})	203	498	13.8
B ₂ (Al ₈₅ Mg _{10.5} Zn _{2.025} Cu _{2.025} Si _{0.45})	255	814	24.8
B ₃ (Al ₉₀ Mg _{7.1} Zn _{1.35} Cu _{1.35} Si _{0.3})	198	794	32.7

where n is the number of the involved elements in an alloy system; r_i denotes the atomic radius; and $\bar{r} = \sum_{i=1}^n c_i r_i$ is the average atomic radius. Zhang et al. proposed a parameter (Ω) to predict the phase formation (Ref 39, 52) as follows:

$$\Omega = \frac{T_m \Delta S_{\text{mix}}}{|\Delta H_{\text{mix}}|} \quad (\text{Eq 6})$$

where $T_m = \sum_{i=1}^n c_i (T_m)_i$ is the average melting temperature of the n -elements HEA; and $(T_m)_i$ is the melting temperature of the i th component. The Pauling electronegativity difference and valence electron concentration were as follows:

$$\Delta\chi = \sqrt{\sum_{i=1}^n c_i (\chi_i - \bar{\chi})^2} \quad (\text{Eq 7})$$

$$VEC = \sum_{i=1}^n c_i (VEC)_i \quad (\text{Eq 8})$$

where $\bar{\chi} = \sum_{i=1}^n c_i \chi_i$, χ_i is the Pauling electronegativity for the i th element; and $(VEC)_i$ is the VEC of the i th element.

Among all of the aforementioned criteria, the atomic size difference (δ) plays a crucial role in phase formations. A large value of δ will indicate low element diffusion and phase formation rates, after which the nanoparticles or amorphous phases are separated out, and the stability of a solid solution becomes broken down. In contrast, small values of δ promote the formations of solid solutions. In fact, a $\delta \leq 6.6\%$ has been considered as a criterion for the formation of solid solution phases in compositionally complex alloys. Zhang et al. summarized δ and ΔH_{mix} in analyzed alloys and after plotting their relationships concluded that solid solutions tend to form in the region of $-22 \text{ kJ/mol} \leq \Delta H_{\text{mix}} \leq 5 \text{ kJ/mol}$.

In this research study, in order to better understand phase formations in the low-density multicomponent alloys, the relationship between δ and the other four criteria was plotted, as detailed in Fig. 5. The corresponding phase constituents were derived from the research conducted by Zhang and Yang (Ref 33) and the value ranges of the criteria were calculated based on Eqs 3 to 8. Yang et al. believed that along with small δ values, the near-zero values of the absolute ΔH_{mix} , large values of Ω (≥ 1.1), and small $\Delta\chi$ (≤ 0.175) effectively favored the stability of solid solutions, rather than those of intermetallic compounds. Therefore, δ - ΔH_{mix} , δ - Ω , and δ - $\Delta\chi$ graphs could be used to predict the solid solution formations for HEAs which were based on $3d$ and/or $4d$ transition metal (TM) elements. Meanwhile, the VEC rule provided a convenient way to design the FCC or BCC HEAs containing mainly $3d$ and/or $4d$ TM elements. It was also pointed out that the configurational entropy was not enough to form a majority of the solid solution phase in low-density alloys containing a mass of Al, Mg, and other light elements. The critical values of the parameters were required to be modified in order to account for the apparent light elements, smaller values of δ ($\delta \leq 4.5\%$), and greater ΔH_{mix} ($-1 \text{ kJ/mol} \leq \Delta H_{\text{mix}} \leq 5 \text{ kJ/mol}$), and Ω ($\Omega > 10$). Meanwhile, the $\Delta\chi$ was determined to be the most predictable parameter across the extensive HEAs. Overall, the intermetallic compounds were determined to be stabilized when $\Delta\chi \geq 0.175$.

As listed in Table 4, the values of the δ , ΔH_{mix} , Ω , VEC , and $\Delta\chi$ were calculated in this study. Then, the relative locations of

those alloys in the δ - ΔH_{mix} , δ - Ω , δ - $\Delta\chi$, and δ - VEC maps were plotted, as detailed in Fig. 5. It was clear these six lightweight alloys were inside the range of “traditional” solid solutions (containing mainly $3d$ and/or $4d$ TM elements), which confirmed that they were not in good agreement with the rules for low-density multicomponent alloys. However, the B_1 , B_2 , and B_3 alloys mainly contained the aluminum element, and almost their α -Al phases are illustrated in Fig. 3(d) to (f). In particular, the B_2 , and B_3 alloys displayed good mechanical behavior fitting with the criteria of δ and ΔH_{mix} . Fortunately, the parameter $\Delta\chi$ was found to seemingly distinguish the solid solution formation behavior most uniformly. According to Yang’s view (Ref 33), the configurational entropy is not sufficient to form the majority of the solid solution phases in low-density alloys containing a mass of Al, Mg, and other main group elements. Therefore, it can be concluded that the δ , ΔH_{mix} , and $\Delta\chi$ should potentially be regarded as the parameters for low-density multicomponent alloys, where $\delta \leq 4.5\%$, $-1 \text{ kJ/mol} \leq \Delta H_{\text{mix}} \leq 5 \text{ kJ/mol}$, and $\Delta\chi \leq 0.175$.

The mixing of enthalpy promotes the formation of the intermetallic compounds, while the mixing of entropy promotes the formation of solid solutions. The values of the mixing enthalpy of binary systems ($\Delta H_{\text{mix}} AB$) are listed in Table 5. The Mg-Si binary system is known to have the most negative mixing of enthalpy (-26 kJ/mol), which means that the bonding force between these two elements is the strongest, and Mg_2Si phase formation often occurs. Thereafter, with the Si element exhausted, the temperatures of molten alloys will be close to the solidification point of the Cu element. The EDS map observed that the Cu element appeared segregated at the grain boundary. This was likely due to the crystallization of a multicomponent eutectic, which included a copper-containing phase. It is interesting to note that the Cu element always occurs at a high content of the Mg element area, with the exception of the Mg_2Si region. This phenomenon may be due to the fact that the mixing enthalpy between the Cu and Mg is higher than the others. The EDS analysis showed that the aluminum elements in the crystal and the grain boundary had the greatest degrees of composition fluctuations. For the main alloying elements, the most serious segregation was the Cu element, followed by the Zn element.

Table 6 details the volume fraction of intermetallic, eutectic, and solid solution phases of the alloys. The fracture strength of the Group A alloys was determined to be linearly related to the eutectic volume fraction, and the linear fitting equation was as follows:

$$y = 334x + 441 \quad (\text{Eq 9})$$

where x is the eutectic volume fraction and y denotes the fracture strength. With the increasing aluminum content, the element ratio reached the eutectic point, and a vast eutectic structure was formed, as shown in Fig. 3(a) and (b). The group of A alloys displayed a brittle fracture mode, and cracks were initiated from the boundary of the intermetallic. The eutectic structure was the mechanical mixture of the $\text{Mg}_{32}(\text{AlZn})_{49}$ intermetallic and a solid solution and displayed a chrysanthemum distribution. The finely dispersed eutectic structure was found to be well distributed in all of the substrates, which was useful in preventing the extension of cracks and increasing strength. The A_2 alloy exhibited the highest σ_f of the Group A alloys, as shown in Fig. 4 and Table 3. When the elemental composition reached the A_3 point, the bulk solid solutions began to precipitate, as shown in Fig. 3(c). Then, with the

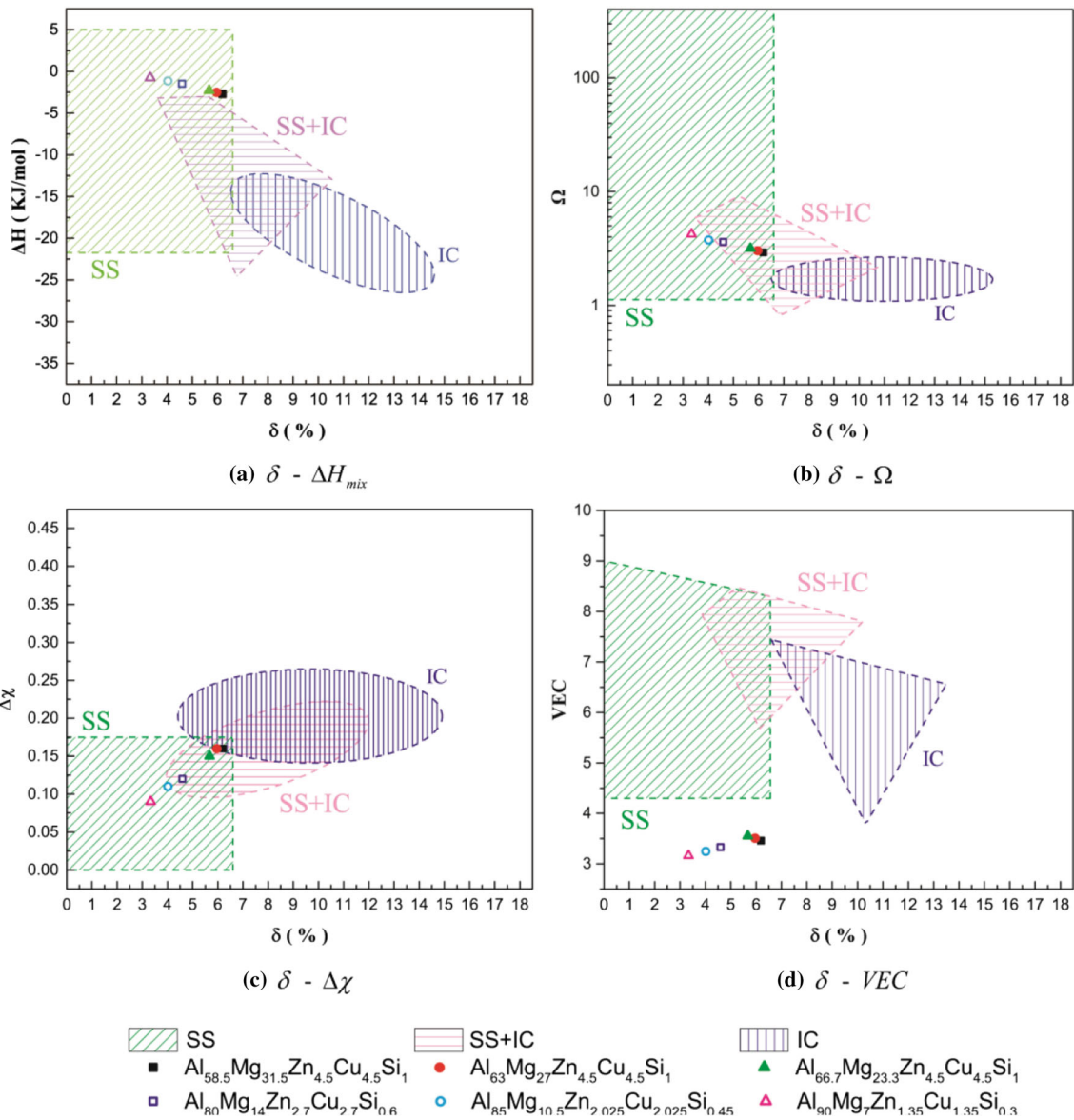


Fig. 5 Phase constituent prediction maps (SS: solid solution; IC: intermetallic compound)

Table 4 Calculated values for δ , ΔH_{mix} , ΔS_{mix} , T_{mix} , Ω , VEC, and $\Delta\chi$ of alloys in this work

Alloys	δ , %	ΔH_{mix} , KJ/mol	ΔS_{mix} , J/mol·k	T_{mix} , K	Ω	VEC	$\Delta\chi$
A ₁ (Al _{58.5} Mg _{31.5} Zn _{4.5} Cu _{4.5} Si ₁)	6.19	-2.70	8.34	945.92	2.92	3.46	0.16
A ₂ (Al ₆₃ Mg ₂₇ Zn _{4.5} Cu _{4.5} Si ₁)	5.96	-2.52	8.06	946.40	3.03	3.51	0.16
A ₃ (Al _{66.7} Mg _{23.3} Zn _{4.5} Cu _{4.5} Si ₁)	5.67	-2.30	7.70	946.90	3.16	3.55	0.15
B ₁ (Al ₈₀ Mg ₁₄ Zn _{2.7} Cu _{2.7} Si _{0.60})	4.59	-1.48	5.65	941.47	3.61	3.33	0.12
B ₂ (Al ₈₅ Mg _{10.5} Zn _{2.025} Cu _{2.025} Si _{0.45})	4.02	-1.16	4.64	939.80	3.75	3.245	0.11
B ₃ (Al ₉₀ Mg _{7.1} Zn _{1.35} Cu _{1.35} Si _{0.3})	3.33	-0.76	3.45	937.48	4.24	3.16	0.09

increasing stress conditions, cracks were initiated and crossed the solid solution, which exhibited high plasticity. At this point, plastic deformation took place. Therefore, the A₃ alloy had displayed a higher ϵ_p than the A₁ and A₂ alloys. The mechanical properties of the Group B alloys were observed to be different from those described above. The fracture strengths and solid solution fractions displayed a parabola

curve relationship when the Al composition reached 80%. The parabola equation was as follows:

$$y = -165x^2 + 2.61 \times 10^4x - 9479 \quad (\text{Eq 10})$$

where x is the solid solution volume fraction and y represents the fracture strength. When the aluminum content reached 80%, the volume fraction of the solid solution was predominant, as

Table 5 Values of enthalpy of mixing ΔH_{mix} AB (kJ mol⁻¹), calculated by Miedema's model for atomic pairs between constitutive elements of Al–Mg–Zn–Cu–Si alloys (in the upper right triangular region) and equilibrium phases for equiatomic binary systems contained in Al–Mg–Zn–Cu–Si alloys at room temperature (in the lower left triangular region)

Elements	Al	Mg	Zn	Cu	Si
Al	...	– 2	1	– 1	– 19
Mg	Al ₂ Mg ₃ + Al ₁₂ Mg ₁₇	...	– 4	– 3	– 26
Zn	Al(Fcc) + Zn(Bcc)	Mg(Hcp) + MgZn	...	1	– 18
Cu	Primitive monoclinic	Cu ₂ Mg + CuMg ₂	B ₂	...	– 19
Si	Al(Fcc) + Si(diamond cubic)	Mg ₂ Si + Si(diamond cubic)	Zn(Fcc) + Si(diamond cubic)	Si(diamond cubic) + Cu ₃ Si	...

Table 6 Volume fractions of intermetallic, eutectic, and solid solution phases in alloy

Alloys	Intermetallic	Eutectic, %	Solid solution, %
A ₁ (Al _{58.5} Mg _{31.5} Zn _{4.5} Cu _{4.5} Si ₁)	34.33%	43.32	22.35
A ₂ (Al ₆₃ Mg ₂₇ Zn _{4.5} Cu _{4.5} Si ₁)	15.48%	73.46	11.06
A ₃ (Al _{66.7} Mg _{23.3} Zn _{4.5} Cu _{4.5} Si ₁)	11.03%	59.77	29.20
B ₁ (Al ₈₀ Mg ₁₄ Zn _{2.7} Cu _{2.7} Si _{0.60})	...	35.35	64.65
B ₂ (Al ₈₅ Mg _{10.5} Zn _{2.025} Cu _{2.025} Si _{0.45})	...	25.75	74.25
B ₃ (Al ₉₀ Mg _{7.1} Zn _{1.35} Cu _{1.35} Si _{0.3})	...	14.90	85.10

shown in Fig. 3(d) to (f), and the Group B alloys displayed a ductile fracture mode. During the process of plastic deformation, a dislocation slip had occurred in the solid solution, and the slip process was blocked when the dislocation extended to the eutectic structure. The eutectic structure was able to impede the movement of the dislocation and also played a very important role in the strengthening of the alloys. It was observed that the more the volume fraction of the eutectic, the higher the σ_f . Also, the eutectic dispersion was found to be more diffuse in the substrate with higher σ_f . Therefore, there was determined to be a maximal influence of the eutectic fraction on the fraction strength. The composition of the B₂ alloy was found to be closest to the maximum, and it also showed the highest σ_f of the Group B alloys.

5. Conclusions

In this research study, a series of lightweight Al–Mg-based entropic alloys were examined in-depth, which had been designed based on the concept of HEAs. It was found that all of the alloys exhibited low densities ranging from 2.64 to 2.75 g/cm³, which were below the density of standard titanium alloys (4.5 g/cm⁻³). The examined alloys consisted of various intermetallic phases and an α -Al solid solution phase in the as-cast state. When the aluminum concentration increased, the volume fraction of the intermetallic was observed to gradually decline, and the α -Al solid solution phase was dominant. The fabricated lightweight HEAs had high strength, with compressive strength exceeding 500 MPa at room temperature. The strength of the B₂ alloy even surpassed 800 MPa. The Al–Mg-rich B₁, B₂, and B₃ alloys displayed excellent plasticity, with high strain to failure values of 13.8, 24.8, and 32.7%, respectively. The critical values of the δ , ΔH_{mix} , Ω , VEC , and $\Delta\chi$ were discussed in this study in order to explain the apparent differences in behavior of the lightweight element compositions. The modified δ , ΔH_{mix} , and $\Delta\chi$ were regarded as the

probable parameters for the lightweight multicomponent alloys, where $\delta \leq 4.5\%$, $-1 \text{ kJ/mol} \leq \Delta H_{\text{mix}} \leq 5 \text{ kJ/mol}$, and $\Delta\chi \leq 0.175$.

Acknowledgments

YZ would like to acknowledge the financial support for this research study provided by the National Natural Science Foundation of China (NSFC, 51471025, 51671020). LS would like to thank Dr. X Yang and Ms DY Li for their technical assistance.

References

- Z. Li, K.G. Pradeep, Y. Deng et al., Metastable High-Entropy Dual-Phase Alloys Overcome The Strength-Ductility Trade-Off, *Nature*, 2016, **534**, p 227–230
- W. Zhang, P.K. Liaw, and Y. Zhang, Science and Technology in High-Entropy Alloys, *Sci. China Mater.*, 2018, **61**(1), p 2–22
- Y. Zhang, T.T. Zuo, Z. Tang et al., Microstructures and Properties of High-Entropy Alloys, *Prog. Mater. Sci.*, 2014, **61**, p 1–93
- J.W. Yeh, S.Y. Chang, Y.D. Hong et al., Anomalous Decrease in X-ray Diffraction Intensities of Cu–Ni–Al–Co–Cr–Fe–Si Alloy Systems with Multi-principal Elements, *Mater. Chem. Phys.*, 2007, **103**, p 41–46
- R.X. Li, P.K. Liaw, and Y. Zhang, Synthesis of Al_xCoCrFeNi High-Entropy Alloys by High-Gravity Combustion from Oxides, *Mater. Sci. Eng. A*, 2017, **707**, p 668–763
- Y. Zou, S. Maiti, W. Steurer et al., Size-Dependent Plasticity in an Nb₂₅Mo₂₅Ta₂₅W₂₅, Refractory High-Entropy Alloy, *Acta Mater.*, 2014, **65**, p 85–97
- Y.J. Zhou, Y. Zhang, Y.L. Wang et al., Solid Solution Alloys of AlCoCrFeNiTi_x with Excellent Room-Temperature Mechanical Properties, *Appl. Phys. Lett.*, 2007, **90**, p 181904–181904-3
- Y. Zhang, G.L. Chen et al., Phase Change and Mechanical Behaviors of Ti_xCoCrFeNiCu_{1-y}Al_y High Entropy Alloys, *J. ASTM Int.*, 2010, **7**, p 1–8
- Y.J. Hsu, W.C. Chiang, and J.K. Wu, Corrosion Behavior of FeCoNiCrCu_x High-Entropy Alloys in 3.5% Sodium Chloride Solution, *Mater. Chem. Phys.*, 2005, **92**, p 112–117
- C.P. Lee, Y.Y. Chen, C.Y. Hsu et al., The Effect of Boron on the Corrosion Resistance of the High Entropy Alloys Al_{0.5}CoCrCuFeNiB_x, *J. Electrochem. Soc.*, 2007, **154**, p C424–C430

11. Z. Tang, L. Huang, W. He et al., Alloying and Processing Effects on the Aqueous Corrosion Behavior of High-Entropy Alloys, *Entropy*, 2014, **16**, p 895–911
12. C.J. Tong, Y.L. Chen, and J.W. Yeh, Mechanical Performance of the $\text{Al}_x\text{CoCrCuFeNi}$ High-Entropy Alloy System with Multiprincipal Elements, *Metall. Mater. Trans. A*, 2005, **36**, p 1263–1271
13. M.R. Chen, S.J. Lin, J.W. Yeh et al., Effect of Vanadium Addition on the Microstructure, Hardness, Wear Resistance of $\text{Al}_{0.5}\text{CoCrCuFeNi}$ High-Entropy Alloy, *Metall. Mater. Trans. A*, 2006, **37**, p 1363–1369
14. C.Y. Hsu, J.W. Yeh, S.K. Chen et al., Wear Resistance and High-Temperature Compression Strength of FCC $\text{CuCoNiCrAl}_{0.5}\text{Fe}$ Alloy with Boron Addition, *Metall. Mater. Trans. A*, 2004, **35**, p 1465–1469
15. M.H. Chuang, M.H. Tsai, W.R. Wang et al., Microstructure and Wear Behavior of $\text{Al}_x\text{Co}_{1.5}\text{CrFeNi}_{1.5}\text{Ti}_x$ High-Entropy Alloys, *Acta Mater.*, 2011, **59**, p 6308–6317
16. Y. Shi, B. Yang, and P.K. Liaw, Corrosion-Resistant High-Entropy Alloys: A Review, *Met. Open Access Metall. J.*, 2017, **7**(2), p 43
17. Y. Shi, B. Yang, X. Xie et al., Corrosion of $\text{Al}_x\text{CoCrFeNi}$ High-Entropy Alloys: Al-Content and Potential Scan-Rate Dependent Pitting Behavior, *Corros. Sci.*, 2017, <https://doi.org/10.1016/j.corsci.2017.02.019>
18. Y. Shi, L. Collins, R. Feng et al., Homogenization of $\text{Al}_x\text{CoCrFeNi}$ High-Entropy Alloys with Improved Corrosion Resistance, *Corros. Sci.*, 2018, <https://doi.org/10.1016/j.corsci.2018.01.030>
19. Y.J. Zhou, Y. Zhang, Y.L. Wang et al., Microstructure and Compressive Properties of Multicomponent $\text{Al}_x(\text{TiVCrMnFeCoNiCu})_{100-x}$ High-Entropy Alloys, *Mater. Sci. Eng. A*, 2007, **s454–455**, p 260–265
20. F.J. Wang, Y. Zhang, G.L. Chen et al., Tensile and Compressive Mechanical Behavior of a $\text{CoCrCuFeNiAl}_{0.5}$ High Entropy Alloy, *Int. J. Mod. Phys. B*, 2012, **23**, p 1254–1259
21. T.T. Shun and Y.C. Du, Age Hardening of the $\text{Al}_{0.3}\text{CoCrFeNiCo}_{0.1}$ High Entropy Alloy, *J. Alloys Compd.*, 2009, **478**, p 269–272
22. O.N. Senkov, G.B. Wilks, J.M. Scott et al., Mechanical properties of $\text{Nb}_{25}\text{Mo}_{25}\text{Ta}_{25}\text{W}_{25}$, $\text{V}_{20}\text{Nb}_{20}\text{Mo}_{20}\text{Ta}_{20}\text{W}_{20}$, Refractory High Entropy Alloys, *Intermetallics*, 2011, **19**, p 698–706
23. A.V. Kuznetsov, D.G. Shaysultanov, N.D. Stepanov et al., Tensile Properties of an AlCrCuNiFeCo High-Entropy Alloy in As-Cast and Wrought Conditions, *Mater. Sci. Eng. A*, 2012, **533**, p 107–118
24. F. Otto, A. Dlouhý, C. Somsen et al., The Influences of Temperature and Microstructure on the Tensile Properties of a CoCrFeMnNi High-Entropy Alloy, *Acta Mater.*, 2013, **61**, p 5743–5755
25. Y. Zhang, T.T. Zuo, Y.Q. Cheng et al., High-Entropy Alloys with High Saturation Magnetization, Electrical Resistivity, Malleability, *Sci. Rep.*, 2013, **3**, p 1455
26. Y.F. Kao, S.K. Chen, T.J. Chen et al., Electrical, Magnetic, Hall Properties of $\text{Al}_x\text{CoCrFeNi}$ High-Entropy Alloys, *J. Alloys Compd.*, 2011, **509**, p 1607–1614
27. K.M. Youssef, A.J. Zaddach, C. Niu et al., A Novel Low-Density, High-Hardness, High-Entropy Alloy with Close-Packed Single-Phase Nanocrystalline Structures, *Mater. Res. Lett.*, 2014, **2**, p 95–99
28. O.N. Senkov, S.V. Senkova, C. Woodward et al., Low-Density, Refractory Multi-Principal Element Alloys of the Cr-Nb-Ti-V-Zr System: Microstructure and Phase Analysis, *Acta Mater.*, 2013, **61**, p 1545–1557
29. O.N. Senkov, S.V. Senkova, D.B. Miracle et al., Mechanical Properties of Low-Density, Refractory Multi-Principal Element Alloys of the Cr-Nb-Ti-V-Zr System, *Mater. Sci. Eng. A*, 2014, **565**, p 51–62
30. R. Feng, M.C. Gao, C. Lee et al., Design of Light-Weight High-Entropy Alloys, *Entropy*, 2016, **18**(9), p 333
31. R. Feng, M.C. Gao, C. Zhang et al., Phase Stability and Transformation in a Light-Weight High-Entropy Alloy, *Acta Materialia*, 2018, <https://doi.org/10.1016/j.actamat.2017.12.061>
32. Y. Qiu, Y.J. Hu, A. Taylor et al., A Lightweight Single-Phase AlTiVCr Compositionally Complex Alloy, *Acta Mater.*, 2017, **123**, p 115–124
33. R. Li, J.C. Gao, and K. Fan, Study to Microstructure and Mechanical Properties of Mg Containing High Entropy Alloys, *Mater. Sci. Forum*, 2010, **650**, p 265–271
34. R. Li, J.C. Gao, and K. Fan, Microstructure and Mechanical Properties of MgMnAlZnCu High Entropy Alloy Cooling in Three Conditions, *Mater. Sci. Forum*, 2011, **686**, p 235–241
35. E.J. Baek, T.Y. Ahn, J.G. Jung et al., Effects of Ultrasonic Melt Treatment and Solution Treatment on the Microstructure and Mechanical Properties of Low-Density Multicomponent $\text{Al}_{70}\text{Mg}_{10}\text{Si}_{10}\text{Cu}_5\text{Zn}_5$ Alloy, *J. Alloys Compd.*, 2016, <https://doi.org/10.1016/j.jallcom.2016.11.305>
36. T.Y. Ahn, J.G. Jung, E.J. Baek et al., Temperature Dependence of Precipitation Behavior of Al-6Mg-9Si-10Cu-10Zn-3Ni Natural Composite and Its Impact On Mechanical Properties, *Mater. Sci. Eng. A*, 2017, **695**, p 45–54
37. T.Y. Ahn, J.G. Jung, E.J. Baek et al., Temporal Evolution of Precipitates in Multicomponent Al-6Mg-9Si-10Cu-10Zn-3Ni Alloy Studied by Complementary Experimental Methods, *J. Alloys Compd.*, 2017, **701**, p 660–668
38. X. Yang, S.Y. Chen, J.D. Cotton et al., Phase Stability of Low-Density, Multiprincipal Component Alloys Containing Aluminum, Magnesium, Lithium, *JOM*, 2014, **66**, p 1–4
39. Y. Zhang, X. Yang, and P.K. Liaw, Alloy Design and Properties Optimization of High-Entropy Alloys, *JOM*, 2012, **64**, p 830–838
40. Y. Zhang, Y.J. Zhou, J.P. Lin, G.L. Chen, and P.K. Liaw, Solid-Solution Phase Formation Rules for Multi-component Alloys, *Adv. Eng. Mater.*, 2008, **10**, p 534–538
41. Y. Zhang and Y.J. Zhou, Solid Solution Formation Criteria for High Entropy Alloys, *Trans. Tech Publ.*, 2007, **561**, p 1337–1339
42. S. Guo and C.T. Liu, Phase Stability in High Entropy Alloys: Formation of Solid-Solution Phase or Amorphous Phase, *Prog. Nat. Sci. Mater.*, 2011, **21**, p 433–446
43. X. Yang and Y. Zhang, Prediction of High-Entropy Stabilized Solid-Solution in Multi-component Alloys, *Mater. Chem. Phys.*, 2012, **132**, p 233–238
44. S. Guo, C. Ng, J. Lu, and C.T. Liu, Effect of Valence Electron Concentration on Stability of FCC or BCC Phase in High Entropy Alloys, *J. Appl. Phys.*, 2011, **109**, p 103505
45. O.N. Senkov, G.B. Wilks, D.B. Miracle et al., Refractory High-Entropy Alloys, *Intermetallics*, 2010, **18**, p 1758–1765
46. O.N. Senkov, J.M. Scott, S.V. Senkova et al., Microstructure and Room Temperature Properties of A High-Entropy TaNbHfZrTi alloy, *J. Alloy. Compd.*, 2011, **509**, p 6043–6048
47. O.N. Senkov and C.F. Woodward, Microstructure and Properties of a Refractory $\text{NbCrMo}_{0.5}\text{Ta}_{0.5}\text{TiZr}$ Alloy, *Mater Sci Eng A*, 2011, **529**, p 311–320
48. J.W. Yeh, S.Y. Chang, Y.D. Hong et al., Anomalous Decrease in X-ray Diffraction Intensities of Cu–Ni–Al–Co–Cr–Fe–Si Alloy Systems with Multi-principal Elements, *Mater Chem Phys*, 2007, **103**, p 41–46
49. J.W. Yeh, S.J. Lin, T.S. Chin et al., Formation of Simple Crystal Structures in Cu-Co-Ni-Cr-Al-Fe-Ti-V Alloys with Multiprincipal Metallic Elements, *Metall. Mater. Trans. A*, 2004, **35**, p 2533–2536
50. Y.J. Zhou, Y. Zhang, Y.L. Wang et al., Solid Solution Alloys of AlCoCrFeNiTi_x with Excellent Room-Temperature Mechanical Properties, *Appl. Phys. Lett.*, 2007, **90**, p 181904–181904-3
51. S.P. Rudman, *Phase stability in metals and alloys*, McGraw-Hill, New York, 1967
52. Q.W. Xing and Y. Zhang, Amorphous Phase Formation Rules in High-Entropy Alloys, *Chin. Phys. B*, 2017, **26**, p 18104–018104